Pergamon

Int. J. Heat Mass Transfer. Vol. 37, No. 3, pp. 511–521, 1994

0017–9310/94 $6.00 + 0.00

Heat transfer in liquid metals with electric currents and magnetic fields: the conduction case†

ALI KAAN KALKAN and GITA TALMAGE
Department of Mechanical Engineering, Pennsylvania State University, University Park, PA 16802, U.S.A.

(*Received* 2 *October* 1992 *and in final form* 19 *March* 1993)

Abstract—There are two volumetric heat sources in a liquid-metal sliding electrical contact for a homopolar device: Joulean heating and viscous dissipation. The Joulean heating is created by the presence of electric currents; the viscous dissipation results from the motion of the liquid metal and is enhanced by magnetohydrodynamic (MHD) effects. In a homopolar device, the liquid metal is confined to a small gap between the perimeter of a rotating disk and the surrounding static surface. The maximum temperature achieved within the liquid metal is significantly larger for an MHD flow than for an ordinary hydrodynamic flow, a flow in the absence of a magnetic field. Information concerning the temperature distribution within the liquid metal and solid parts of a homopolar device will result in the design of efficient and operational sliding electrical contacts.

1. INTRODUCTION

HEAT TRANSFER in liquid metals with electric currents and magnetic fields differs considerably from heat transfer in electrically insulating fluids and in conducting solids, because both Joulean heating and viscous dissipation act as volumetric heat sources. Whether the viscous dissipation or Joulean heating dominates depends on, among other parameters, the total current as well as the strength and orientation of the magnetic field [1]. Unlike ordinary hydrodynamic (OHD) flows, the velocity field is determined, in part, by the electromagnetic (EM) body forces, $\mathbf{j}^* \times \mathbf{B}^*$, and the current density is determined, in part, by the induced electric field, $\mathbf{u}^* \times \mathbf{B}^*$. Here, $\mathbf{j}^*$ is the dimensional electric current density, $\mathbf{u}^*$ is the dimensional velocity and $\mathbf{B}^*$ the dimensional flux density of the local magnetic field. As a consequence, the viscous dissipation is increased over that for OHD flows due to the MHD-enhanced velocity gradients. There are instances in which the Joulean heating and viscous dissipation are so large that significant temperature gradients arise in spite of the large thermal conductivity of liquid metals. One example of this phenomenon occurs in liquid-metal sliding electrical contacts for homopolar machines. With large electric currents and strong magnetic fields, large temperature gradients develop within a small region of liquid metal.

Homopolar generators and motors are high-current, low-voltage, DC electromechanical energy converters. Typically, solid copper disks (or rotors) are mounted on a shaft, and the tip of each rotor is shrouded by a stationary copper surface (or stator). Sliding electrical contacts, which provide low-resistance current paths between the rotor tips and shrouding stators, may carry DC current densities in excess of 10^7 A m^{-2} between the outer periphery of each rotor and stator surface. A liquid metal, such as the eutectic mixture of sodium and potassium (NaK), in the narrow gap between the rotor tip and concentric stator surface acts as a sliding electrical contact. Since NaK has a large electrical conductivity, $\sigma = 2.4 \times 10^6$ S m^{-1}, and a small dynamic viscosity, $\mu = 6.5 \times 10^{-4}$ Pa s^{-1}, a liquid-metal sliding electrical contact has an extremely low electrical resistance, produces very little drag on the disk because of its low viscosity and forms an excellent electrical contact with copper. When the disk begins to rotate, the liquid metal is carried by viscous drag to fill the gap around the entire periphery of the disk. As the speed increases, centrifugal forces produce a relatively uniform distribution of liquid around the periphery.

While NaK is an excellent electrical and thermal conductor, its electrical conductivity is still roughly one-thirtieth that of solid copper, and electric current densities of 10^7 A m^{-2} produce considerable Joulean heating in each sliding electrical contact. The viscous dissipation, which is associated with a typical velocity change of 90 m s^{-1} across a gap of 0.1 mm and the very large shear rates in the electromagnetically driven fluid motions, can be comparable to the Joulean heating. For a typical motor-generator set, the Joulean heating and viscous dissipation in the liquid-metal sliding electrical contacts generally account for roughly half the total losses. The heat generated in the liquid metal must be transported through the stator and/or rotor to coolant channels. A number of recent studies have determined the liquid-metal motion, Joulean heating and viscous dissipation in sliding electrical contacts with arbitrary levels of electric current

† The opinions and conclusions are solely those of the authors and do not necessarily reflect the opinions and conclusions of the U.S. Government.

NOMENCLATURE

a	dimensionless width of the free surface
b	dimensionless half-width of the rotor face
B	magnitude of the flux density of the local magnetic field
h	electric current density stream function
I	total dimensionless electric current per unit length
$\mathbf{j}$	electric current density vector
k	thermal conductivity
L	dimensional length of the radial gap
M	Hartmann number
N	interaction parameter
Pe_s	Peclet number
R	dimensionless rotor radius
R_m	magnetic Reynolds number
s	dimensionless width of the side stators
T	temperature
t_R	dimensionless length between the rotor tip and the coolant channel
t_S	dimensionless thickness of the axial stator
$\mathbf{u}$	velocity vector
x	azimuthal coordinate
y	radial coordinate
z	axial coordinate.

Greek symbols

ε	small convergence parameter
η	coordinate aligned with the magnetic field
θ	angle between the local magnetic-field vector and the y-axis
κ	the thermal diffusivity
μ	dynamic viscosity
μ_p	magnetic permeability
ν	kinematic viscosity
ρ	density
σ	electrical conductivity
ϕ	electric potential function
Ω	angular velocity of the rotor.

Subscripts

LM	liquid metal
R	rotor
S	stator.

Superscript

*	a dimensional quantity.

between the rotor and stator and with local magnetic fields of arbitrary strength and orientation [1–4]. However, the temperature distribution associated with the heat transfer from the liquid metal, through the rotor and stator, to the coolant channels was not previously determined. In this paper, we will present results for the temperature distribution. To understand the nature of the temperature distribution, we need to consider the magnetic field, the liquid-metal motion and the current density distribution.

Superconducting magnet coils produce a non-uniform, skewed magnetic field with radial and axial components. The liquid-metal region of each sliding electrical contact is so small that the local magnetic field can be treated as uniform. However, a homopolar machine usually has more than one contact, each with different local magnetic-field orientations. The electric currents in the solid parts produce a small azimuthal magnetic field which we neglect. In the liquid metal, the characteristic ratio of the induced magnetic field to the applied magnetic field is the magnetic Reynolds number, $R_m = \mu_p \sigma \Omega L^2 R$, where μ_p, Ω, L, and R are the magnetic permeability, the angular velocity of the rotor, the radial distance between the concentric rotor and stator surfaces, and the ratio of the rotor radius to L, respectively. Since a typical value of R_m is 0.03, we neglect the induced magnetic field. Therefore the applied magnetic field, which is uniform, has arbitrary radial and axial components.

A non-axisymmetric MHD flow can develop due to two mechanisms: an irregular concentric stator surface and gravitational field effects. An irregular stator surface creates a variation in the primary velocity in the azimuthal direction [5]. All solid surfaces treated here are taken to be smooth so that they do not induce a non-axisymmetric flow. Gravitation causes, at most, a small perturbation in the axisymmetric flow for the typical parameters of a liquid-metal sliding electrical contact [2]. Therefore, we neglect gravitational effects and treat only axisymmetric flows in which all variables are independent of the azimuthal coordinate.

The axisymmetric liquid-metal consists of a primary flow involving the azimuthal velocity and a secondary flow involving the radial and axial velocities. The primary flow is driven by the rotor-surface motion and by the EM body force due to the magnetic field and the electric currents between the rotor and stator. The radial and axial components of the electric current density produce an azimuthal EM body force either in the direction of rotor rotation or in the opposite direction. The azimuthal velocity produces a radial centrifugal force which drives the secondary flow. The radial and axial velocities interact with the magnetic field to drive an azimuthal electric current which produces an EM body force opposing the secondary flow. While the azimuthal velocity is always comparable to the rotor-tip velocity, $U = \Omega RL$, the characteristic secondary-flow velocity,

$$U_s = \frac{\rho\Omega^2 RL}{\sigma B^2} = \frac{\rho\Omega}{\sigma B^2} U,$$

is obtained by equating the centrifugal force, $\rho(\Omega RL)^2/RL$, to the EM body force opposing the secondary flow, $\sigma U_s B^2$. The density of the liquid metal is denoted by ρ.

Two key dimensionless parameters that govern the flow are the Hartmann number M and the interaction parameter N, defined by

$$M = BL\sqrt{\left(\frac{\sigma}{\rho\nu}\right)}, \quad N = \frac{\sigma^2 B^4}{\rho^2\Omega^2 R}.$$

M^2 and N are the characteristic ratios of the EM body force to the 'viscous force' and 'inertial force', respectively. With this definition of the interaction parameter, $U_s = U/\sqrt{(NR)}$. Since the flow is axisymmetric, the only convection of both primary and secondary-flow momentum is due to the secondary flow which diminishes as the magnetic field strength increases. For large values of N, the magnitudes of the primary flow variables are significantly greater than the magnitudes of the secondary flow variables, and the secondary-flow momentum transport can be neglected. In other words, the primary azimuthal motion is decoupled from the secondary flow and is fully developed. The only inertia term that remains is the centrifugal force, which appears in the radial momentum equation. For liquid-metal sliding electrical contacts, the interaction parameter is sufficiently large that the $N \gg 1$ approximation is valid [6]. Two previous papers [2, 3] present primary-flow solutions for $N \gg 1$ and for various combinations of magnetic-field orientation, Hartmann number and net electrical current between the rotor and stator. We use the results of these past efforts to calculate the Joulean heating and viscous dissipation.

For the heat transfer problem, there is an additional parameter, the Peclet number. Since the temperature distribution is also axisymmetric, the Peclet number is based on the characteristic velocity of the secondary flow:

$$Pe_s = \frac{U_s L}{\kappa} = \frac{UL}{\sqrt{(NR)}\kappa}$$

where κ is the thermal diffusivity of the liquid metal. In spite of the small thermal diffusivity for NaK ($\kappa \approx 2.6\times10^{-5}$ m^2 s^{-1} at 100°C), for stronger magnetic-field strengths and for the lower limit of typical operating speeds, Pe_s is sufficiently small that secondary-flow heat transport, or convection, is neglected.

The three dimensionless parameters, the flow regime, the orientation of the magnetic field, and the electric potential difference across the rotor gap (which defines the total current) determine the temperature distribution. The strength of the magnetic field, which also plays a role in determining the temperature distribution, can be taken into account through the Hartmann number: the stronger the magnetic-field strength, the larger the Hartmann number.

The flow regime for a typical homopolar device ranges from laminar to turbulent, depending on the rotor tip velocity. While the essential characters of the temperature distribution is not dependent on the flow regime, there are significant differences. Under similar operating conditions (i.e. total current and magnetic-field orientation and strength), the temperature gradients and the maximum temperature for a turbulent flow are typically smaller than for a laminar flow. These changes can be attributed to turbulent mixing which dramatically reduces the peak velocity and the velocity gradients within the central core region of the liquid metal [3, 4]. Near the rotor tip and concentric stator surface the velocity gradients increase. The net result, however, is a decrease in the total viscous dissipation, below its laminar value. Because the laminar flow regime generally gives rise to larger maximum temperatures and temperature gradients than does the turbulent flow regime, this paper treats the laminar flow regime only.

The definition of the magnetic field orientation and the electric potential difference across the rotor gap are intimately tied to the geometry. Therefore, before discussing these parameters, a description of a model of the liquid-metal sliding electrical contact for a homopolar device is necessary. The radius of the rotor is significantly larger than the rotor gap, i.e. $R \gg 1$, so the problem may be treated in a Cartesian coordinate system (Fig. 1). With the origin at the center of the axial stator surface, the y-axis points radially inward, the z-axis is axial, and the x-axis is in the azimuthal direction. The dimensionless length of the rotor face is $2b$. Liquid metal is confined to the radial gap region which has a dimensionless height of one. The dimensionless thickness of each stator side is s, while the radial distances from the liquid metal to the coolant channels in the rotor and stator are t_R and t_S, respectively. We will assume a known location

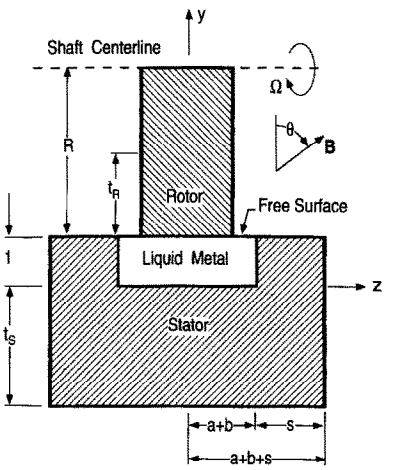

FIG. 1. Geometry of a model liquid-metal sliding electrical contact.

for the free surface, $y = 1$. The free surfaces extend from the sides of the rotor to the stationary side walls (the side stators), and the dimensionless length of each free surface is a.

The orientation of the magnetic field is defined in terms of θ which represents the angle between the local magnetic-field vector and the y-axis. For different sliding electrical contacts in a homopolar device, the local magnetic-field orientation varies from radial ($\theta = 0$) to axial ($\theta = \pi/2$ rad). The magnetic field is normalized by B, so that the dimensionless magnetic field is given by $\mathbf{B} = \cos\theta\hat{\mathbf{y}} + \sin\theta\hat{\mathbf{z}}$, where $\hat{\mathbf{x}}$, $\hat{\mathbf{y}}$ and $\hat{\mathbf{z}}$ are unit vectors.

The electrical conductivity of the solid parts is significantly greater than the electrical conductivity of the liquid metal. Therefore, we will take the solid parts to be perfect electrical conductors. The electric potential is set to zero at the stator surfaces ($y = 0$ for $|z| \leqslant (a+b)$ and $|z| = (a+b)$ for $0 \leqslant y \leqslant 1$). From Ohm's law, the axial component of the current density is zero along the rotor tip ($y = 1$, for $|z| \leqslant b$). Consequently, the axial component of the electrostatic electric field balances the axial component of the induced electric field due to the motion of the rotor across the magnetic field, i.e.

$$\frac{\partial\phi}{\partial z} = \cos\theta, \quad \text{at} \quad y = 1, \quad \text{for} \quad |z| \leqslant b,$$

where ϕ is the dimensionless electric potential function and the dimensionless primary azimuthal velocity u is one at $y = 1$. Integrating this relation with respect to z, we obtain $\phi = \phi_0 + z\cos\theta$ at $y = 1$, for $|z| \leqslant b$, where ϕ_0 is the electric potential at $y = 1$, $z = 0$ and represents the average dimensionless voltage difference across the rotor gap.

The last set of parameters that influence the temperature distribution are the transport properties. If the temperature differences are not too large, as a first approximation, the transport properties can be considered constant. This paper treats a steady, laminar axisymmetric MHD flow with arbitrary Hartmann number, large interaction parameter, small Peclet number and constant transport properties. Section 2 describes the problem formulation and the numerical analysis used to obtain the temperature distribution. Section 3 presents the results of a parametric study involving θ and ϕ_0, and Section 4 provides a discussion of those results.

2. PROBLEM FORMULATION AND NUMERICAL ANALYSIS

The governing equations are comprised of the Navier–Stokes equations, conservation of mass, conservation of energy, Maxwell's equations, and Ohm's law. For liquid metals, which are incompressible, the energy equation decouples from the other equations if the transport properties are constant. Therefore, the velocity field and the current densities are determined prior to the temperature field.

As discussed in Section 1, the primary, azimuthal flow is driven by the motion of the rotor, while the secondary flow is driven by the centrifugal force. The radial and axial current densities, which are associated with the primary azimuthal flow, are normalized by σUB. The azimuthal current density, a secondary-flow quantity, is normalized by $\sigma U_s B$. From these nondimensionalizations,

$$j_x^* = \frac{\sigma UB}{\sqrt{(NR)}} j_x, \quad j_y^* = \sigma UB j_y, \quad j_z^* = \sigma UB j_z,$$

where the superscript * denotes a dimensional parameter and j_x, j_y and j_z are the electric current densities directed azimuthally, radially inward and axially, respectively. From this and statements made in Section 1, we may conclude that for large values of N, the magnitudes of the primary flow variables are significantly greater than the magnitudes of the secondary flow variables. Therefore, the secondary-flow quantities can be neglected.

With the geometry and assumptions given, the dimensionless governing equation for the temperature distribution within the liquid metal is

$$\frac{\partial^2 T_{\mathrm{LM}}}{\partial y^2} + \frac{\partial^2 T_{\mathrm{LM}}}{\partial z^2} = -M^{-2}\left[\left(\frac{\partial u}{\partial y}\right)^2 + \left(\frac{\partial u}{\partial z}\right)^2\right] - [j_y^2 + j_z^2] \quad (1)$$

where T_{LM} denotes the dimensionless temperature of the liquid metal. The temperature is normalized by

$$T_{\mathrm{LM}}^* - T_0 = \frac{\sigma(\Omega RL)^2 B^2 L^2}{k} T_{\mathrm{LM}}$$

where T_{LM}^* is the dimensional liquid metal temperature, T_0 is the temperature at the wall of the coolant channel, and k is the thermal conductivity of the liquid metal. The terms that appear on the right-hand-side of equation (1) represent the viscous dissipation,

$$M^{-2}\left[\left(\frac{\partial u}{\partial y}\right)^2 + \left(\frac{\partial u}{\partial z}\right)^2\right],$$

and the Joulean heating, $j_y^2 + j_z^2$. There is no Joulean heating within the solid parts because they have been assumed to be perfect electrical conductors. Furthermore, with the assumption that the transport properties are constant, the temperature distribution equation within both the rotor and stator is governed by Laplace's equation,

$$\frac{\partial^2 T_{\mathrm{S,R}}}{\partial y^2} + \frac{\partial^2 T_{\mathrm{S,R}}}{\partial z^2} = 0. \quad (2)$$

Here, the subscript S denotes the stator, R the rotor, and

$$T_{\mathrm{S,R}}^* - T_0 = \frac{\sigma(\Omega RL)^2 B^2 L^2}{k} T_{\mathrm{S,R}}.$$

We will assume that the cover gas is a thermal insulator so that

$$\frac{\partial T_{LM}}{\partial y} = 0, \quad \text{at} \quad y = 1, \quad \text{for} \quad |b| < z < |a+b|.$$

This assumption is reasonable since the thermal conductivity of the liquid metal is two to three orders of magnitude larger than that of the cover gas, e.g. $k \approx 24.4$ W m^{-1} K^{-1} for NaK at approximately 100°C and $k \approx 0.021$ W m^{-1} K^{-1} for argon at approximately 100°C. At the interface of the liquid metal and the stator or rotor, the temperature and heat flux are continuous. For example, at the liquid-metal–rotor interface,

$$T_{LM} = T_R, \quad k\frac{\partial T_{LM}}{\partial y} = k_R \frac{\partial T_R}{\partial y},$$

$$\text{at} \quad y = 1, \quad \text{for} \quad |z| \leqslant b,$$

where k_R is the thermal conductivity of the rotor. The side walls of the rotor, the external side walls of the stator, and the stator walls at $y = 1$ are thermal insulators. The dimensionless temperature difference is set to zero at $y = t_S$ for $|z| \leqslant (a+b+s)$ and at $y = 1+t_R$ for $|z| \leqslant b$.

The governing equations together with the boundary conditions form a well-posed problem which was solved using a full numerical technique. We introduce a mesh which is non-uniform in both y and z using trigonometric functions [4]. The spatially differenced versions of equations (1) and (2) are solved using a Gauss–Seidel relaxation method. The convergence criterion is based on the difference between the new iteration and the previous iteration:

$$\sum_j \sum_k |T^n_{j,k} - T^{n-1}_{j,k}| \leqslant \varepsilon$$

where the summations are taken over the entire discretized domain, $(\ )^n$ represents the current iteration, $(\ )^{n-1}$ represents the previous iteration, $T_{j,k}$ is the dimensionless temperature difference at $y = y_j$ and $z = z_k$, and ε is a small number, typically 10^{-7}. Once this type of convergence criterion is achieved, the residuals are calculated to ensure that the governing equations are indeed satisfied. In all cases treated, the solution converged rapidly, and the residuals were small, $O(10^{-7})$. In addition, we refine the spatial grid until the results are independent of the grid spacings.

Given that no experimental data are available for this problem, we tested our results using a second numerical technique. We chose a hybrid method [7] that matches a numerical solution in the liquid metal and side stators (where $0 \leqslant y \leqslant 1$, for $|z| \leqslant (a+b+s)$) with an analytical solution in the axial stator and rotor. The results from the full numerical solution were in excellent agreement with the results from the hybrid solution.

3. RESULTS

Here we consider the effects of varying the total current and the magnetic-field orientation on the temperature distribution. A Hartmann number of five is chosen for all cases. It represents an intermediate value within the parameter range for liquid-metal sliding electrical contacts. Increasing the Hartmann number would result in larger EM body forces which would drive larger velocities and produce larger current densities. This would cause an increase in the viscous dissipation and Joulean heating and a subsequent increase in the maximum temperature and in the temperature gradients.

The total current is determined, in part, by ϕ_0, which represents the dimensionless voltage drop across the rotor gap. There is a special case with $I = 0$, where I is the total dimensionless current per unit length of channel. This case is termed the no-load case. $I = 0$ does not imply that there are no currents, but rather that the net or total current is zero. The average electrostatic electric field then balances the average induced electric field: $\nabla\phi = \hat{\mathbf{x}} \times (\cos\theta\hat{\mathbf{y}} + \sin\theta\hat{\mathbf{z}})$. With $\phi = \phi_0 + z\cos\theta$ along the rotor tip and $\phi = 0$ at the stator walls, we encounter three distinct possibilities when $I = 0$.

- With a radial magnetic field, $\theta = 0$ and $\phi = \phi_0 + z$ along the rotor tip. If ϕ_0 is set to zero, the net voltage difference across the rotor gap is zero. However, for $z > 0$, $\phi = z > 0$ along the rotor tip, and current flows from the rotor to the stator; for $z < 0$, $\phi = z < 0$, and current flows from the stator to the rotor. The Joulean heating is non-zero, in spite of the fact that the total current is zero.
- With an axial magnetic field, $\theta = \pi/2$ and $\phi = \phi_0$, a constant, along the rotor tip. From a one-dimensional analysis [1], $\phi_0 = -0.5$ for $I = 0$. For the two-dimensional problem, $\phi_0 = -0.48$, which is slightly smaller than -0.5 because currents fringe at the rotor corners giving a smaller average j_y. With $\phi_0 < 0$, if there is any current, it flows from the stator to the rotor because the electric potential is constant along $y = 1$ for $|z| \leqslant b$. However, with $I = 0$, the average electrostatic electric field is balanced by the average induced electric field, leaving j_y essentially zero. If there is any current, it will fringe at $y = 1$, $z = \pm b$ and will result in a small j_z that is positive for $z = -b$ and negative for $z = +b$. The Joulean dissipation will be small.
- With a skewed magnetic field, say $\theta = \pi/4$, $\phi = \phi_0 + z/\sqrt{2}$. For a zero total current, $\phi_0 = -0.1535$. This possibility is similar to the radial field case in that there is an eddy current: current flows from the rotor to the stator for $z > 0.2171$ and from the stator to the rotor for $z < 0.2171$, but the total current is zero. Here, too, the Joulean dissipation is non-zero. The eddy currents represent a loss of productive electrical power and are to be avoided.

What distinguishes the radial field case from a skewed field case is that the Joulean dissipation is maximum for the radial field case. Therefore, the radial field represents the worst possible case in terms of lost productive electrical power. To understand why the Joulean dissipation is larger for the radial field

case we must consider how the eddy current is calculated. For a sufficiently large magnetic-field strength, current flows along magnetic-field lines. The distance that currents travel from the rotor tip to the axial stator surface is sec θ. This length is a minimum when $\theta = 0$. If we let η represent the coordinate that is parallel to magnetic-field lines, j_η the η-component of the electric current density and ϕ_R the value of the electric potential at the rotor tip for a specifeid value for η, then

$$j_\eta = -\frac{\partial\phi}{\partial\eta} = -\frac{\Delta\phi}{\Delta\eta} = -\frac{\phi_R}{\sec\theta}.$$

The eddy current is the product of $|j_\eta|$ with the cross-sectional area through which the electric current density flows. The cross-sectional area is proportional to $\cos\theta$. Therefore, the eddy current is proportional to $\cos^2\theta$ and is a maximum for $\theta = 0$.

For all the results presented, the ratio of the thermal conductivity of the solid parts to the liquid metal is 15, $a = 3.12$, $b = 9.88$, $s = 3.5$, $t_R = 2.0$, and $t_S = 3.1$. Furthermore, because the aspect ratio of the rotor gap is 26:1, the radial axis has been stretched by a factor of two for the temperature distribution contour lines and by a factor of ten for the velocity and current density stream function contour lines. The entire computational domain $[-t_S \leqslant y \leqslant 1+t_R, |z| \leqslant (a+b+s)]$ is used in the figures for the temperature distribution, and only the liquid-metal region is shown for the velocity and current density stream function contour lines.

Variations with total current

We consider two values of I for $\theta = 0$: $I = 0$, the no-load case, and $I = -100$, where the current flows from the rotor to the axial stator. The isotherms for $I = 0$ and $I = -100$ are shown in Figs. 2(a) and (b), respectively. For $I = 0 (\phi_0 = 0)$, the dimensionless temperature ranges from zero at the coolant channels (at $y = -t_S$, for $|z| \leqslant (a+b+s)$ and at $y = 1+t_R$, for $|z| \leqslant b$) to 15.66 at $y = 0.5$, $z = \pm 9.35$. The isotherms are symmetric about $z = 0$. The temperature is not constant in the central core region but is $O(10^{-1})$. The contour levels are too coarse to plot temperatures of this magnitude. The same type of problem occurs in the solid parts, where the temperatures are not constant but too small for the contour lines to be resolved. In the solid parts, there are no volumetric heat sources. Energy is transferred to these parts from the liquid metal via conduction. With the thermal conductivity of the solid parts an order of magnitude larger than that of the liquid metal and the only source of energy to the solid parts coming from the liquid metal, the temperature within the solid parts is significantly smaller than the maximum temperature in the liquid metal. It is seen from Fig. 2(a) that the temperature is continuous at the liquid-metal–solid interface but that the temperature gradients are not. The discontinuity in the gradients arises because the thermal conductivity of the liquid metal does not equal the thermal conductivity of the solid parts. For $I = -100$, the minimum temperature is again zero at the coolant channels. The maximum temperature, located at

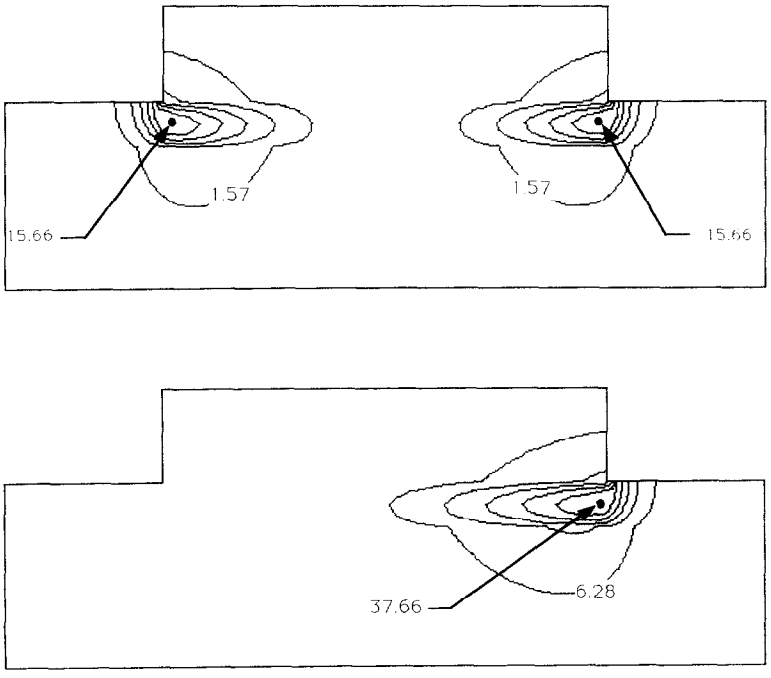

FIG. 2. Isotherms for $I = 0$ and $I = -100$ with $\theta = 0$. (a) $I = 0$: Contour intervals are 2.61. (b) $I = -100$: Contour intervals are 6.28.

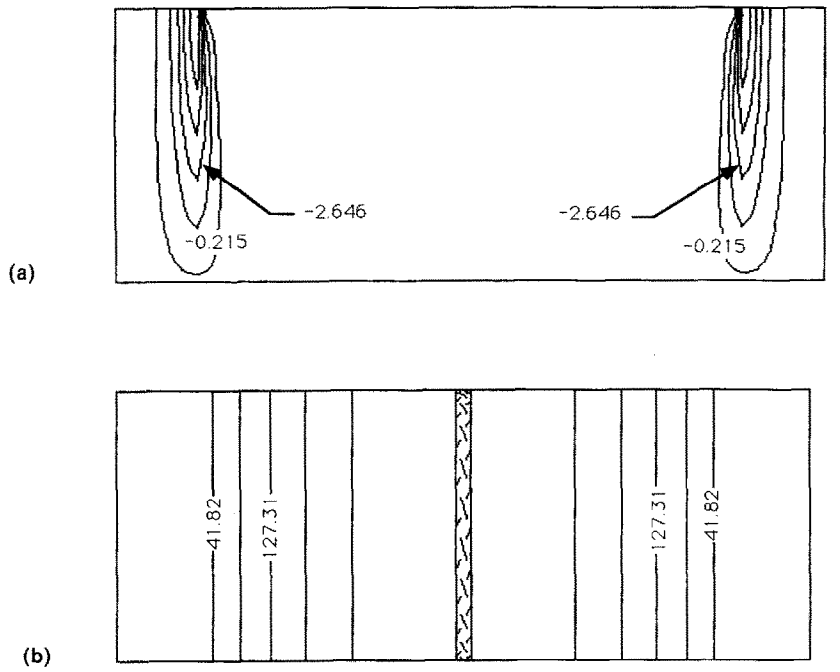

FIG. 3. Velocity and current density stream line contours for $I = 0$ and $\theta = 0$. (a) Velocity contour lines: contour intervals are 1.215. (b) Current density stream line contours: contour intervals are 42.76.

$y = 0.5, z = 9.35$, is 37.66. The isotherms are not symmetric about $z = 0$. The temperature is not constant in the left-half of the domain, but the contour levels are too coarse to distinguish these isotherms. In fact, the character of the isotherms on the left-half is very similar to that on the right-half, but the magnitudes of the temperature in the left-half are significantly less with a maximum temperature of approximately 3.3

The behavior of the velocity and the current density determine the viscous dissipation and Joulean heating, which in turn govern the temperature distribution. Therefore, knowledge of the nature of the velocity and the current density is essential. Figure 3(a) represents the velocity contour lines in the liquid metal for $I = 0$. The velocity distribution in the central core is characteristic of Couette flow, $u = y$. These contour lines do not appear in Fig. 3(a). With a uniform velocity gradient equal to one, there is uniform viscous dissipation within the core region. Two symmetric interior layer jets flow in the minus x-direction with peak velocities of -6.29. These jets are symmetric because the electric potential along the rotor tip is antisymmetric: $\phi(1, z) = z$, for $|z| \leqslant b$ [2]. The viscous dissipation is large at the center of the velocity jets and near the rotor corners, where the velocity gradients are large. The current density stream lines, defined as

$$j_y = M^{-1}\frac{\partial h}{\partial z} \quad \text{and} \quad j_z = -M^{-1}\frac{\partial h}{\partial y},$$

are vertical throughout the core region, indicating that the current density in the z-direction is zero (Fig. 3(b)). Therefore, the current density is aligned with the magnetic field, and, as a consequence, there are no EM body forces in the core region. Without an EM body force, the flow must be pure Couette flow, as it is. The current density stream lines show that $j_y(-z) = -j_y(+z)$ with $j_y > 0$ for $z < 0$ and $j_y < 0$ for $z > 0$. Although Fig. 3(b) does not show any fringing of current density stream function lines, there is a slight fringing of these lines near both rotor corners. The fringing is due to the discontinuity in the gradient of the electric potential. It is this fringing that drives the interior layer jets. The Joulean heating is largest where the current densities are a maximum, near the rotor corners. The isotherms in Fig. 2(a) are symmetric because the viscous dissipation and the Joulean heating are themselves symmetric about $z = 0$.

For $I = -100$, the velocity contour lines and the current density stream lines, which are not shown, are not symmetric about $z = 0$. The electric potential along the rotor tip is now $\phi(1, z) = \phi_0 + z = 5.0 + z$. At $z = \pm b$, $\phi = 14.88$ and -4.88, respectively, so the electric potential difference at $z = +b$ dominates. The flow in the central core region remains a Couette flow, and the velocities in the two interior layers are still in the minus x-direction. But, now, the magnitude of the velocity in the right interior layer is significantly greater than the magnitude of the velocity in the left interior layer, and the velocity gradients are very large in the center of the right velocity jet. The current density stream lines are still parallel to the magnetic field in the central core region, but more current passes

through the region $-5 < z \leqslant (a+b)$ than through $-(a+b) \leqslant z < -5$.

For both $I = 0$ and -100, the hot spots are not located at the rotor corners, $y = 1$, $z = \pm b$ but at $y = 0.5$ and $z = \pm 9.35$. The total dimensionless viscous dissipation, P_μ, increases from 279 to 343 and the total dimensionless Joulean heating, P_j, from 1.67×10^4 to 2.93×10^4 when I goes from zero to -100. The total viscous dissipation and the total Joulean heating are normalized by $2\pi R\mu U^2$ and defined as

$$P_\mu = \int_{-(a+b)}^{(a+b)} \int_0^1 \left[\left(\frac{\partial u}{\partial y} \right)^2 + \left(\frac{\partial u}{\partial z} \right)^2 \right] \mathrm{d}y \, \mathrm{d}z$$

and

$$P_j = M^2 \int_{-(a+b)}^{(a+b)} \int_0^1 (j_y^2 + j_z^2) \, \mathrm{d}y \, \mathrm{d}z.$$

The Joulean heating is nearly 60 times larger than the viscous dissipation for $I = 0$ and 85 times larger for $I = -100$. In these two cases, the Joulean heating dominates.

Variations with the magnetic-field orientation

As the magnetic-field orientation varies from radial to axial, the total viscous dissipation and total Joulean heating behave as indicated in Table 1. These results are for $I = 0$. The total Joulean heating decreases as θ increases. However, the total viscous dissipation does not: P_μ is largest at $\theta = \pi/4$, the skewed magnetic field. With a radial magnetic-field orientation, the velocity field (Fig. 3(a)) is comprised of three distinct flow patterns: Couette flow in the central core region with a uniform velocity gradient, jet-like regions under each rotor corner with large velocity gradients, and a stagnant region near the side stators with small velocity gradients. At the other extreme, an axial field, the flow is essentially Couette flow, with uniform velocity gradients. The region between the rotor corners and the side stators has larger velocity gradients as the side stators retard the flow. The velocity contour lines for a skewed magnetic field (Fig. 4(b)) have the jet-like regions and the stagnant regions that are seen in the radial field case, but the central core region differs significantly. For a sufficiently strong radial magnetic field, there is no EM body force in the central core region or in the Hartmann layer at $y = 1$. (A Hartmann layer is similar to the boundary layer in an OHD flow.) For a sufficiently strong skewed magnetic field, there is no EM body force in the central core region, but a large EM body force is created in the Hartmann layer. The current in the core region is aligned with the magnetic field, which is at some angle to the y-axis. The solid parts are treated as a perfect electrical conductors, therefore current must enter perpendicularly to the rotor tip. In other words, the current density can have only a radial component as it enters the rotor at $y = 1$. So, as the current passes through the Hartmann layer, it crosses magnetic field lines, creating an EM body force. The EM body force is in the positive azimuthal direction near $z = -b$, reinforcing the viscous effects of the rotor motion. As z increases toward the origin, the EM body force decreases. Eventually, the EM body force is in the negative azimuthal direction, cancelling the effect of the rotor motion. The velocity is large and in the positive azimuthal direction near $z = -b$ and is large and negative near $z = +b$. The gradients are not uniform nor are they particularly small. Within both free shear layers, the velocity is in the negative azimuthal direction. Consequently, when the core velocity near $z = -b$ encounters the free shear layer velocity, large gradients develop. Near $z = +b$, the core velocity and the free shear layer velocity reinforce each other, also creating large velocity gradients. The result is that the viscous dissipation is larger for a skewed magnetic field than for a radial magnetic field.

Table 1.

θ	P_j	P_μ
0	1.67×10^4	279.1
$\pi/4$	5.11×10^3	958.1
$\pi/2$	6.00×10^{-1}	22.7

The isotherms for $\theta = \pi/4$ and $I = 0$ are shown in Fig. 4(a). These isotherms do not appear to be radically different from the radial magnetic field isotherms. Two hot spots exist: one centered under each rotor corner. In the left hot spot, the maximum temperature, approximately 7.9, occurs near the rotor corner, and in the right hot spot, the maximum temperature, approximately 4.7, occurs near $y = 0.5$. The temperature distribution in the region between the hot spots is not constant, but it is an order of magnitude smaller than the temperature within the hot spots. In the side stators, as $|z|$ goes from $(a+b)$ to $(a+b+s)$, the temperature, which is an order of magnitude smaller than in the hot-spots, decreases. Again, the behavior of the velocity and the current density stream function determine the structure of the isotherms.

The nature of the velocity contours and the current density stream lines shown in Figs. 4(b), (c) have been discussed previously [2], so details will not be provided here. What is most relevant to the temperature distribution problems is that the viscous disssipation is greatest near the left interior layer and in the right 'jet' region. In the central core region the velocity is a superposition of a Couette flow and an electromagnetically driven flow, and the magnitude of the velocity gradients is not as large as it is in the regions near the rotor corners. Near the side stators, $|z| = (a+b)$, the flow is essentially stagnant, so there is little viscous dissipation. The current density stream function exhibits a similar behavior with the Joulean dissipation greatest near the rotor-corner–free-surface interface. Based on these contours, the isotherms should be most concentrated in the left interior layer and in the right 'jet' region. Figure 4(a) bears this out.

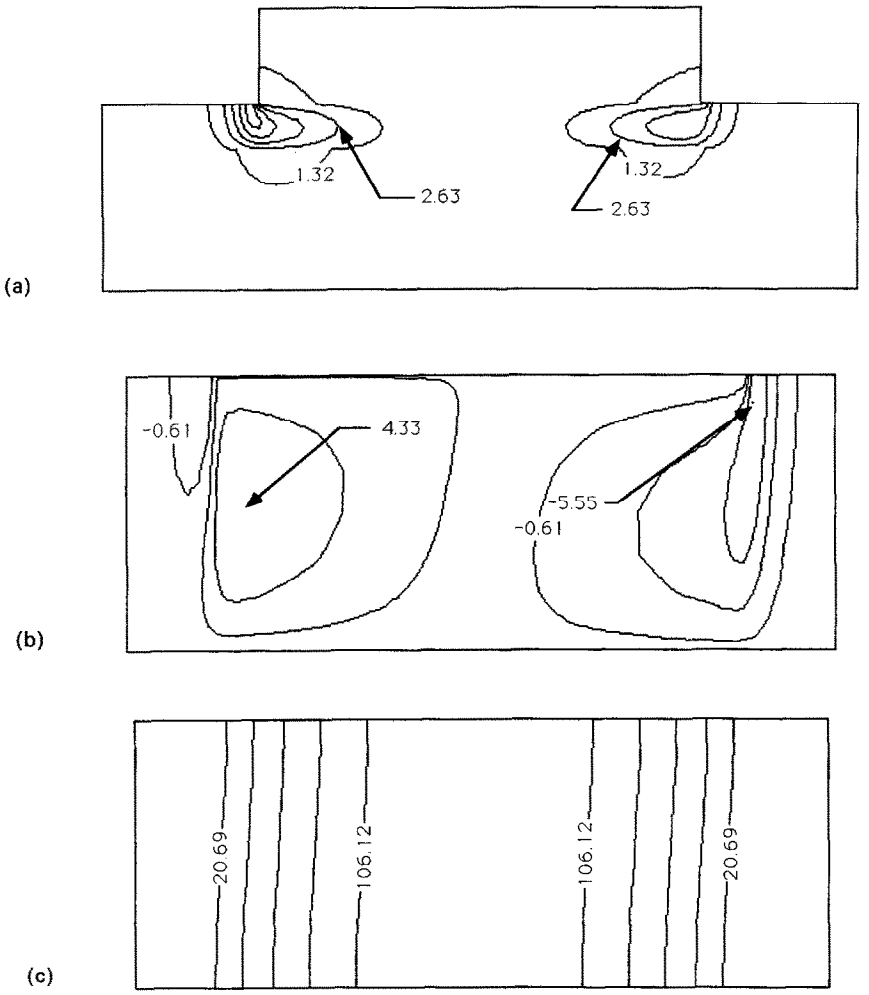

FIG. 4. Temperature, velocity and current density stream function distributions for $I = 0$ and $\theta = \pi/4$. (a) Isotherms: contour intervals are 1.32. (b) Velocity contour lines: contour intervals are 1.65. (c) Current density stream line contours: contour intervals are 21.36.

The temperature distribution within the liquid metal and solid parts for $\theta = \pi/2$ and $I = 0$ is shown in Fig. 5(a). In the central core region, the temperature distribution is a parabolic function of y. The magnitude of the temperature decreases away from $y = 0.5$. If we were to consider a one-dimensional analysis, for the no-load case ($\phi_0 = -0.5$)

$$T(y) = \frac{M^{-2}y^2}{2} + Ay + B$$

where the coefficients A and B can be determined from the temperatures at $y = 0$ and $y = 1$. The first term $M^{-2}y^2/2$ is associated with the viscous dissipation. For the axial field case $j_y = 0$, and there is no contribution to the temperature distribution from Joulean heating. The results from the one-dimensional solution agree with the results from the two-dimensional solution. As we move outward toward the rotor corners, the temperature distribution loses its parabolic character and the temperature becomes larger near $z = \pm b$. The maximum temperature is 0.0129 at $y = 1$, near the rotor corners. Towards the stator sidewalls, near the free surface, the temperature distribution is essentially a linear function of z since the free surface is a thermal insulator, $\partial T_{LM}/\partial y = 0$.

Again, the behavior of the velocity and the current density determine the temperature distribution. (We will not present figures of the velocity and current density contour lines.) The velocity distribution in the central core region is characteristic of Couette flow with a uniform velocity gradient equal to one. Toward the stator sidewalls, the flow is retarded by the presence of the walls. As a consequence, larger velocity gradients develop. However, even larger velocity gradients evolve near the rotor corners as a result of the velocity discontinuity: at the rotor face, the velocity is one, and at the free surface the normal derivative of the velocity is zero. Therefore, viscous dissipation is largest near the rotor corners. The current is essentially zero in the core region. But, near the rotor corners, the electric potential gradient discontinuity at $y = 1$, $|z| = b$ causes the current density

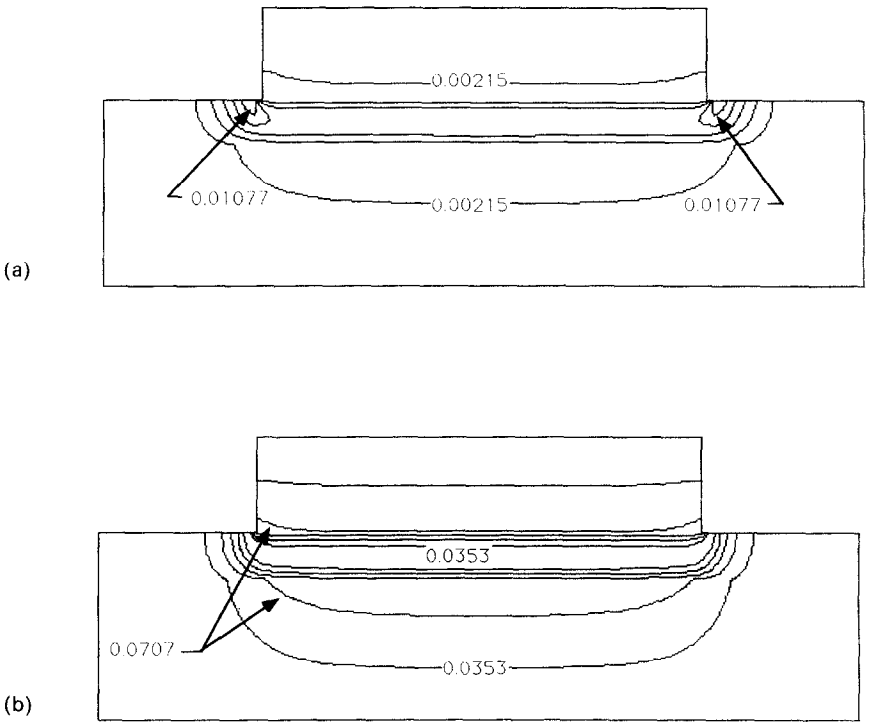

FIG. 5. Effects of Joulean heating on the temperature distribution. (a) Isotherms for $I = 0$ and $\theta = \pi/2$. The contour intervals are 2.15×10^{-3}. (b) OHD isotherms. The contour intervals are 3.53×10^{-2}.

stream function to fringe, and relatively small currents are generated. The result is that Joulean heating, although still very small, is maximum near the rotor corners.

The regions near the rotor corners are the primary source of viscous dissipation and Joulean heating when $\theta = \pi/2$. Due to the retarding effect of the side stators, regions near $|z| = \pm(a+b)$, for $0 < y < 1$, provide some viscous dissipation and Joulean heating but not to the same degree as do the rotor corner regions. As expected, the isotherms are most concentrated in the rotor corners and the side-stator–free-surface regions, with the maximum temperature occurring near the rotor corners.

To illustrate the effects of Joulean heating, consider a steady, laminar OHD flow whose sole volumetric heat source is due to viscous dissipation. The isotherms for the OHD case are shown in Fig. 5(b). The maximum temperature is 0.215 near the rotor corner at $y = 1$. The geometry in the OHD case is the same as in the MHD case. The ratio of the electric conductivities of the solid parts to the fluid also remains the same, 15. The isotherms look quite similar to those in Fig. 5(a) where $\theta = \pi/2$ and $I = 0$. This is to be expected because the velocity profiles are so similar. A Couette velocity profile exists in the central core region. Larger velocity gradients develop near the rotor corners due to the retarding effects of the side walls. In order to compare OHD to the MHD temperature values, we must consider the dimensional temperature.

4. DISCUSSION AND CONCLUSIONS

The non-dimensionalization used for the temperature is

$$T^*_{LM} - T_0 = \frac{\sigma(\Omega RL)^2 L^2 B^2}{k} T_{LM}$$

where T^*_{LM} denotes the dimensional temperature. Typical parameter values are: $\sigma = 2.38 \times 10^6$ S m^{-1} at 311 K, $k = 22$ W m^{-1} K^{-1} (the average value of the thermal conductivity between 20 and 100°C), $\Omega RL = 90$ m s^{-1}, and B is between 0.5 and 6 T. With these typical values, $T^*_{LM} - T_0 = 8.76B^2 T_{LM}$, where the results are in °C. For $B = 0.83$ T, $T^*_{LM} - T_0 = 5.98 T_{LM}$°C. For an OHD flow,

$$T^*_{LM} - T_0 = \frac{\mu(\Omega RL)^2}{k} T_{LM}.$$

With the dynamic viscosity $\mu = 6.5 \times 10^{-4}$ Pa s^{-1}, $T^*_{LM} - T_0 = 0.239 T_{LM}$°C. The dimensional temperature difference at the maximum dimensionless temperature and with $B = 0.83$ T is 93.7°C for $\theta = 0$ and $I = 0$; 225.3°C for $\theta = 0$ and $I = -100$; 15.7°C for $\theta = \pi/4$ and $I = 0$; and 0.06°C for $\theta = \pi/2$ and $I = 0$. For an OHD flow, the dimensional temperature difference is 0.05°C for $T_{LM_{max}} = 0.215$. The saturation temperature for NaK is $T_{SAT} = 825$°C at 760 mm Hg. If $T_0 = 20$–100°C, $T^*_{LM_{max}}$ is far below T_{SAT} when $B = 0.83$ T. For $\theta = 0$, a substantial temperature difference of over 200°C is seen for $I = -100$. The maximum dimensional temperature difference is

slightly larger for the MHD flow with $\theta = \pi/2$, $I = 0$ than for the OHD flow. This is the expected result since the velocity gradients are enhanced by the MHD effects.

The dimensional results presented here are for a relatively small magnetic field strength. The dimensional temperature difference is proportional to the square of the magnetic-field strength, so for the larger magnetic field strengths it is quite possible that $T^*_{LM_{max}}$ exceeds T_{SAT}. We are confronted with two problems. First, as the temperature differences increase, the assumption that the transport properties are not functions of temperature becomes weak. Second, if $T^*_{LM_{max}} > T_{SAT}$, then the flow is not a single-phase flow but a two-phase flow.

In 1978, Talmage and Walker [8] demonstrated that, given large temperature differences, the velocity and temperature distributions differ substantially for constant transport properties and temperature-dependent transport properties in a one-dimensional Hartmann flow. For liquids, as the temperature increases, the density, dynamic viscosity and electrical conductivity decrease and the thermal conductivity increases. Therefore, it is not possible to predict the temperature distribution without actually performing an analysis. The problem itself is further complicated by the fact that the governing equations for the primary azimuthal velocity and the electric potential function cannot be decoupled from the energy equation. Therefore, the velocity, electric potential and the temperature must be calculated simultaneously or iteratively. In addition, the governing equations for the electric potential in the rotor and stator will not reduce to Laplace's equation as was the case for constant temperature transport properties. Fortunately, data for the transport properties as functions of temperature are readily available [9].

If the temperature differences are sufficiently large that $T^*_{LM} > T_{SAT}$, the problem must be treated as a two-phase flow which for MHD problems adds considerable complexity.

In the radial field case, $I = -100$ corresponds to a dimensional current of -3336 A, which is a moderate electric current by the standards of homopolar devices. For those liquid-metal sliding electrical contacts that operate in the presence of a radial magnetic field, even for moderate magnetic-field strengths and electric currents, the temperature differences that develop within the liquid metal can be significant. These large temperature gradients at the rotor corners have the potential for creating significant thermal stresses at the rotor corners. For strong magnetic fields and large electric currents, the temperature differences are substantially larger, with the possibility that the flow is no longer a single-phase flow.

Acknowledgements—The help and advice of Professor J. S. Walker were deeply appreciated. This research was sponsored by Defense Advanced Research Projects Agency (DOD), Naval Technology Office, Submarine Technology Program.

REFERENCES

1. G. Talmage, J. S. Walker, S. H. Brown, N. A. Sondergaard and P. Burt, Magnetohydrodynamic liquid-metal flows in a rectangular channel with an axial magnetic field, a moving conducting wall and free surfaces, *J. Appl. Phys.* **68**(9), 4446–4460 (1990).
2. G. Talmage, J. S. Walker, S. H. Brown and N. A. Sondergaard, Liquid-metal flows in current collectors for homopolar machines: fully-developed solutions for primary azimuthal velocity, *Phys. Fluids* **A1**(7), 1268–1278 (1989).
3. G. Talmage, J. S. Walker, S. H. Brown, N. A. Sondergaard, H. Branover and S. Sukoriansky, Liquid-metal flows in sliding electrical contacts with arbitrary magnetic-field orientations, *Phys. Fluids* **A3**(6), 1657–1665 (1991).
4. G. Talmage, J. S. Walker, S. H. Brown, N. A. Sondergard, H. Branover and S. Sukoriansky, Liquid-metal flows in sliding electrical contacts: solutions for turbulent primary azimuthal velocity, *Prog. Astronaut. Aeronaut.* **149,** 165–189 (1993).
5. D. J. Beatty, J. S. Walker, S. H. Brown and N. A. Sondergaard, Liquid-metal Couette flow with a two-dimensional periodic static surface and with a transverse magnetic field, *J. Appl. Phys.* **72**(2), 367–373 (1992).
6. G. Talmage, J. S. Walker, S. H. Brown and N. A. Sondergaard, Transition from steady to periodic liquid-metal magnetohydrodynamic flow in a sliding electrical contact, *Phys. Fluids* **A5**(9), 2287–2294 (1993).
7. T. J. Moon and J. S. Walker, Liquid metal flow through a sharp elbow in the plane of a strong magnetic field, *JFM* **213,** 397–418 (1990).
8. G. Talmage and J. S. Walker, Hartmann flow with temperature dependent properties, *Dev. Theor. Appl. Mech.* **9,** 393–401 (1978).
9. W. J. O'Donnell, P. G. Papanikolaou and C. B. Reed, The thermophysical and transport properties of NaK near room temperature, Argonne National Laboratory Report, ANL/FPP/TM-237 (February 1989).